High-order exceptional points and stochastic resonance in pseudo-Hermitian systems

Shirin Panahi,[1] Li-Li Ye,[1] and Ying-Cheng Lai[1, 2, *]

[1] *School of Electrical, Computer, and Energy Engineering, Arizona State University, Tempe, AZ 85287, USA*

[2] *Department of Physics, Arizona State University, Tempe, Arizona 85287, USA*

(Dated: November 1, 2024)

Exceptional points, a remarkable phenomenon in physical systems, have been exploited for sensing applications. It has been demonstrated recently that it can also utilize as sensory threshold in which the interplay between exceptional-point dynamics and noise can lead to enhanced performance. Most existing works focused on second-order exceptional points. We investigate the stochastic dynamics associated with high-order exceptional points with a particular eye towards optimizing sensing performance by developing a theoretical framework based on pseudo-Hermiticity. Our analysis reveals three distinct types of frequency responses to external perturbations. A broad type of stochastic resonance is uncovered where, as the noise amplitude increases, the signal-to-noise ratio reaches a global maximum rapidly but with a slow decaying process afterwards, indicating achievable high performance in a wide range of the noise level. These results suggest that stochastic high-order exceptional-point dynamics can be exploited for applications in signal processing and sensor technologies.

I. INTRODUCTION

Non-Hermitian systems arise commonly in physical systems, quantum or classical. For example, when a quantum system is placed in an environment or a "bath" with mutual interactions with the surroundings, the energy of the system is no longer conserved and it becomes non-Hermitian [1–6]. From a mathematical point of view, an imaginary part of the eigenenergy emerges, making it complex [7–14]. One approach to achieving real eigenenergies in a non-Hermitian system is by introducing pseudo-Hermiticity. Historically, the concept of pseudo-Hermiticity was first studied by Dirac and Pauli [15] and was further developed by Mostafazadeh [16–18], who exploited pseudo-Hermiticity to define general conditions for the real spectrum: $UHU^{-1} = H^{\dagger}$, where U is a linear Hermitian operator. For non-Hermitian quantum systems with energy dissipation, the fundamental governing equation is the master equation in the Lindblad formalism [19, 20]. Experimentally, the originally infinite sharp energy levels in the closed system become broadened, leading to various resonances with a finite width [21], which are characteristic features of non-Hermitian quantum systems. Due to the equivalence between the Schrödinger equation and the classical wave equations [22, 23], non-Hermiticity of different physical origins can also arise in a variety of classical systems, such as classical electric circuits with Joule heating [24–27] and photonics devices with gain and loss of photons described by the Maxwell equations [28, 29].

A remarkable phenomenon in non-Hermitian physical systems is the occurrence of exceptional points (EPs) [30–32]. An EP is the point in the parameter space at which n ($n \geq 2$) eigenvalues of the non-Hermitian Hamiltonian matrix and their eigenstates coalesce and emerge as a branch-point singularity. A low-order or second-order EP is referred to as $n = 2$, while $n \geq 3$ defines a high-order EP. An EP differs from a diabolic point in conventional spectral analysis at which some eigenvalues are degenerate, but not their associated eigenstates. In sensor applications based on photonic, acoustic, or electronic systems exhibiting resonances [25, 33–35], EPs can be exploited to amplify the sensitivity [36] of the sensor, a feat that cannot be achieved through a diabolic point. In particular, for a diabolic point, when a perturbation or a weak signal of the strength $\varepsilon \ll 1$ is applied to the system, the splitting of the energy or frequency measured in the transmission or reflection spectrum is proportional to ε. However, for an EP, the energy splitting can be $\varepsilon^{1/(n-1)}$. The higher the order of an EP, the more sensitive the sensor response. The enhancement of the system response about an EP provides a physical mechanism to optimize the sensitivity of the sensors based on detecting the frequency splitting, such as microcavity sensors [36, 37], optical gyroscopes [38], weak magnetic field sensors [39, 40], and nanomechanical mass sensors [41–43].

In the study of EPs, the symmetries of the system play an important role [44]. In non-Hermitian physical systems, the parity-time (PT) symmetry is fundamental. For example, in a hard-core Bose gas modeled by the Toda lattice [45] with the Fermi's pseudopotential [46], the PT symmetry can produce the entire real spectrum in the non-Hermitian matrices [47]. A spontaneous PT symmetry breaking [48, 49] occurs when some eigenstates of the Hamiltonian are not the eigenstates of the PT operator, making some pairs of eigenvalues complex conjugate to each other and generating the PT-broken phase. In this case, a second-order EP emerges between the PT-exact and PT-broken phases. The low-order EP with PT symmetry can be realized in a variety of physical and engineering systems, e.,g., as gain-loss structures in optics [50–53], electronics [54–56], microwaves [57],

* Ying-Cheng.Lai@asu.edu

mechanics and acoustics [58, 59], superconducting circuits [60–62], as well as spin [63] and atomic systems [64]. These systems provide rich experimental settings for investigating various phenomena associated with low-order EPs, such as unidirectional invisibility [65, 66], sensitivity measurement [67, 68], and Berry phase induced from encircling EPs [3, 69–71].

While high-order EPs exhibit merits over low-order EPs such as sensitivity [33, 72, 73], spontaneous emission enhancement [74], and certain topological characteristics [75–77], experimental implementation of high-order EPs with the PT symmetry is challenging [26, 78]. For example, to generate a third-order EP, in between gain and loss resonators, a neutral resonator is required [26, 79]. To realize such a device, completely lossless and gainless features are needed, with equal coupling between the adjacent resonators. Accordingly, pseudo-Hermitian structures without the PT symmetry was proposed [26, 29] to generate high-order EPs in a cavity optomechanical system, which only requires gain and loss elements. Such a design somewhat relaxes the constraint and provides more freedom in the design of high-order EP based sensors. With the state-of-the-art experimental technologies, high-order EPs in pseudo-Hermitian systems have begun to be realized in cavity magnonics [80], cavity optomechanical systems [26, 29, 81], photonic Lieb lattices [82], and the Su-Schrieffer-Heeger chain [83].

The interplay between noise and EP dynamics has attracted recent attention. The phenomenon of stochastic EP was uncovered recently in a sensor system with the PT symmetry and a second-order EP [27]. In particular, with a weak periodic signal as the input, the sensory threshold fluctuates with random PT-phase transitions, suggesting that noise can serve to enhance the sensor performance. This work [27] thus built up a bridge between EP dynamics and the paradigmatic and extensively studied phenomenon of stochastic resonance [84, 85], where noise can be used to optimize the system's response to weak signals in terms of measures such as the signal-to-noise ratio (SNR). So far, this connection has been explored for second-order EP systems with the PT symmetry.

In this paper, we investigate stochastic high-order EP dynamics in pseudo-Hermitian systems. To make feasible experimental implementation, we generalize the necessary conditions for stochastic low-order EP [27] in terms of the complex relation between the system's eigenfrequencies and external disturbance by introducing a more general physical framework for high-order EPs. We identify three distinct types of frequency responses of the system to perturbations, suggesting that stochastic high-order EP can be exploited for designing highly sensitive and robust sensors. Our main finding is the emergence of a remarkable skewed stochastic resonance: as the noise amplitude increases, the SNR increases and reaches the maximum rapidly, followed by a significantly slow decay. The implication is that a wide range of the noise level can be used to achieve the optimal or near optimal SNR. While this is akin to the phenomenon of stochastic resonance without tuning [86, 87], we note that the latter typically occurs in spatially extended dynamical systems that presents a challenge for experimental implementation as sensors. To our knowledge, our stochastic high-order EP system represents a class of non-spatially-extended systems in which an extensive stochastic resonance can arise.

A relevant question is how the SNR depends on the signal amplitude. To address this question, we note that a purpose of generating an EP is for its use as a sensory threshold in scenarios that involve weak periodic signals. About an EP, the system can be highly sensitive to small perturbations, and this sensitivity plays a crucial role in the SNR. In particular, the sensor can be so designed that the weak periodic input signal is "at" or "below" the sensory threshold. This means that, in the absence of noise, the signal would not be strong enough to produce an output response. However, when noise is introduced into the system, it can induce random transitions, thereby enhancing the sensor's performance. We thus have the characteristics of the phenomenon of a stochastic resonance, where noise can "push" the signal beyond the threshold, allowing an output event to be detected. The noise strength is critical, as it determines how frequently and by how much the signal exceeds the threshold, thus impacting the SNR. While the SNR depends on the noise strength, the relationship also hinges on the interplay between noise and the signal amplitude, with certain noise levels optimizing sensor performance and maximizing the SNR. In particular, the dependency of the SNR on the signal amplitude is closely tied to the noise level, especially before or at an EP that acts as a sensory threshold. For signals with such an amplitude, the output amplitude increases with the rising noise level. However, this does not necessarily improve the output signal. If the noise level surpasses a certain threshold, the output becomes dominated by noise, thereby losing the meaningful signal information. Overall, the optimal conditions for maximizing the SNR are contingent upon maintaining a balanced noise level that is sufficient to enhance the signal without overwhelming it and causing degradation.

II. HIGH-ORDER EXCEPTIONAL POINTS

A. Basics

The types of physical systems in which EPs arise are generally open and are described by a non-Hermitian Hamiltonian. To be concrete, we consider a system represented by an $n \times n$ effective Hamiltonian matrix H_0 and a parameter ε characterizing some perturbation $\hat{H}$ to the system. The total Hamiltonian is $H = H_0 + \hat{H}(\varepsilon)$, whose eigenvalues determine the system's response to the perturbation. The resultant eigenvalue splittings represent measurable output quantities accessible through a

spectral analysis. Figure 1 schematically illustrates the real and imaginary parts of the eigenvalues as a function of ε for a system with EP. In particular, because of the non-Hermitian nature of the Hamiltonian, the eigenvalues ω are generally complex, where the real and imaginary parts characterize the frequency and the linewidth of the system response, respectively. For values of ε in an open interval, the eigenvalues are typically distinct. An EP is the value of ε at which both the real and imaginary parts of the eigenvalues coalesce, as shown in Fig. 1.

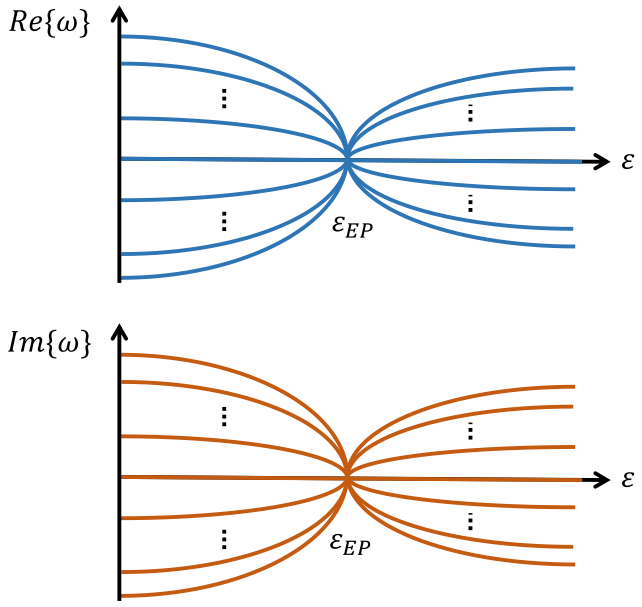

FIG. 1. Schematic illustration of the real (top) and imaginary (bottom) components of the eigenvalues as a function of the perturbation ε. The critical value of the perturbation at which the eigenvalues and corresponding eigenvectors of the system coalesce is ε_{EP}.

Let $\mathrm{Re}\{\delta\omega\}$ and $\mathrm{Im}\{\delta\omega\}$ be the real and imaginary parts of the eigenvalue splittings, respectively. The Q factor of the system, defined as

$$Q = \mathrm{Re}\{\delta\omega\}/(2\mathrm{Im}\{\delta\omega\}),$$

is often used as an index in resonator circuits, which indicates the sharpness of the dip within the measured reflection-spectrum curve. In general, a larger real part and/or a smaller imaginary part of the eigenfrequency spitting can lead to a larger Q factor, yielding higher spectral resolution. Experimentally, the eigenfrequency with the smallest imaginary part corresponds to the sharpest detectable reflection spectral dip.

B. Scenarios for emergence of high-order exceptional points

As the magnitude of the perturbation changes, there are three common scenarios through which an EP can arise: branch, monotonic, and non-injective.

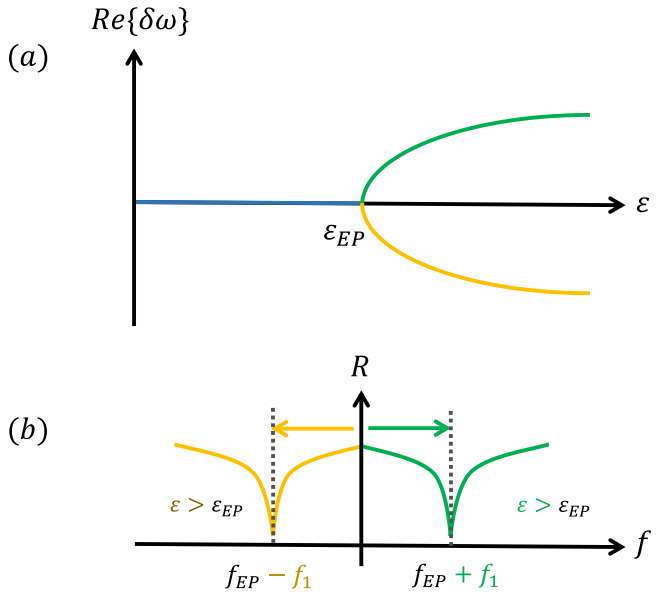

FIG. 2. Emergence of an EP through a branch structure. (a) Real part of frequency splitting $\mathrm{Re}\{\delta\omega\}$ versus the magnitude ε of the perturbation, where an EP arises at ε_{EP}. (b) Consequence of the EP: for $\varepsilon \gtrsim \varepsilon_{EP}$, a pair of dips in the reflection coefficient are created at $f_{EP} \pm f_1$, where f_1 is the absolute value of $\mathrm{Re}\{\delta\omega\}$ at $\varepsilon \gtrsim \varepsilon_{EP}$ in (a).

a. Branch scenario. This scenario arises when the system exhibits a branch-like response to the perturbation, as illustrated in Fig. 2. At the critical bifurcation point ε_{EP}, all the eigenvalues and their corresponding eigenvectors coalesce. For $\varepsilon < \varepsilon_{EP}$, the real part of the splitting of the eigenvalue with the smallest imaginary part, $\mathrm{Re}\{\delta\omega\}$, is constant. For $\varepsilon > \varepsilon_{EP}$, $\mathrm{Re}\{\delta\omega\}$ has two possible values with opposite signs, which are symmetric to each other with respect to the ε-axis, as shown in Fig. 2(a).

To give a physical example, consider an open cavity that reflects and transmits an incoming wave and the quantities of interest are the reflection and transmission coefficients as a function of the frequency. A small positive deviation from the critical point ε_{EP} toward the right will simultaneously lead to a positive and negative shift in the frequency: $\pm\mathrm{Re}\{\delta\omega\}$, giving rise to two dips in the reflection coefficient at $f_{EP} \pm f_1$, respectively, as shown in Fig. 2(b). Accordingly, at each of the two dips, the transmission coefficient exhibits a peak.

Monotonic scenario. In this scenario, as the perturbation is strengthened, the system's frequency response changes monotonically, as illustrated in Fig. 3, where there is a critical saddle point at ε_{EP}. For ε deviating from ε_{EP}, the real part of the eigenvalue with the smallest imaginary part does not split but shifts by a small amount with its sign depending on whether the pertur-

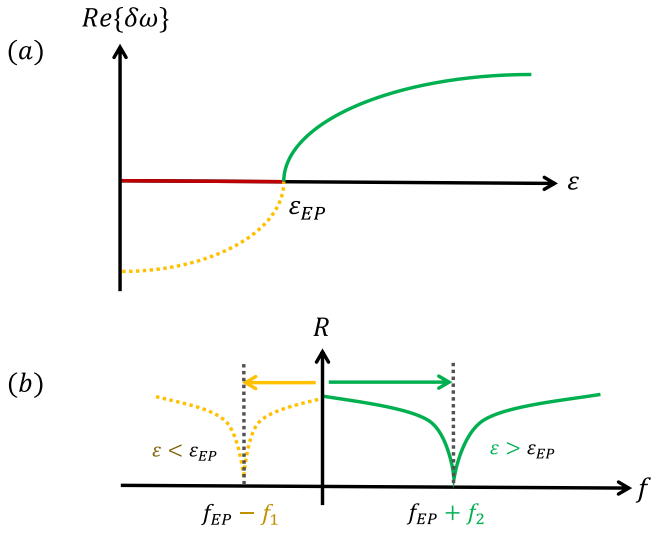

FIG. 3. Monotonic scenario. (a) Real frequency shift Re$\{\delta\omega\}$ versus the perturbation about the critical value ε_{EP}. Depending on whether ε is below or above ε_{EP}, the amount of the shift is negative or positive, respectively. (b) The resulting dips in the reflection coefficient, one for $\varepsilon < \varepsilon_{EP}$ and another for $\varepsilon > \varepsilon_{EP}$. Frequency filtering can be employed to remove a dip.

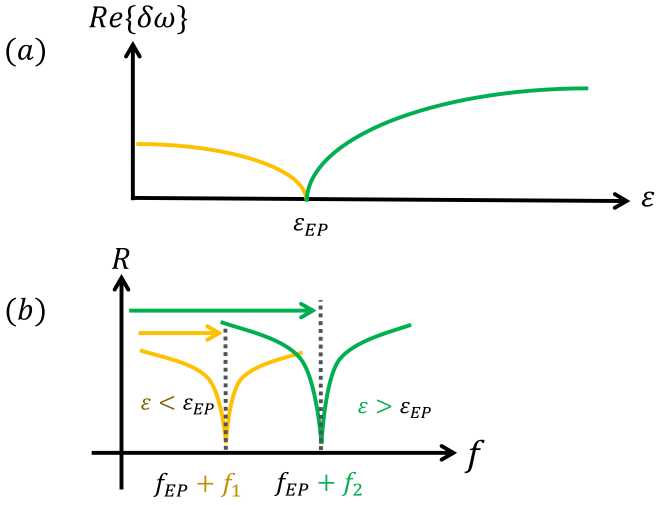

FIG. 4. A non-injective structure. (a) Real frequency splitting Re$\{\delta\omega\}$ for different perturbations. (b) A schematic illustration of the response of a system in terms of the reflection coefficient under a perturbation. Any perturbation leads to a frequency shift to the right. An example for $\varepsilon < \varepsilon_{EP}$ ($\varepsilon > \varepsilon_{EP}$) is shown in yellow (green).

bation is smaller or larger than ε_{EP}. In particular, for $\varepsilon \lesssim \varepsilon_{EP}$, the frequency shift Re$\{\delta\omega\}$ is negative but it is positive for $\varepsilon \gtrsim \varepsilon_{EP}$, as shown in Fig. 3(a). In this case, a perturbation smaller or larger than ε_{EP} result in two distinct values of Re$\{\delta\omega\}$ with opposite signs, leading to two asymmetric dips in the spectrum of the reflection coefficient, one below and another above f_{EP}, as shown in Fig. 3(b). Because of the monotonic behavior of Re$\{\delta\omega\}$ with respect to variations of the perturbation, it is possible to extract the system response from one side of the EP. For example, a filter can be employed to remove the frequency response of the system to perturbations smaller than ε_{EP}, as shown by the dash-dotted curve in Fig. 3(a), leaving the frequency response unchanged in spite of the perturbation (represented by the red solid line).

Non-injective Structure. Figure 4 shows the non-injective structure of the system response to the applied perturbation with respect to an EP or the bifurcation point at ε_{EP}. The system lacks the injective properties, i.e., there is no one-to-one mapping between the distinct elements of its output domain and those of the input domain. In particular, Fig. 4(a) illustrates that the system's response is nearly symmetric around the EP. Figure 4(b) schematically illustrates two examples of the response of the system in terms of the reflection coefficient, which indicate a rightward shift in both cases. As a result, distinguishing between the response corresponding to $\varepsilon < \varepsilon_{EP}$ (yellow) and $\varepsilon > \varepsilon_{EP}$ (green) becomes infeasible.

In general, in a non-injective structure, the response of the system is approximately symmetric with respect to the EP, so both larger and smaller perturbations can cause a similar shift in the frequency spectrum. As a result, it becomes difficult to distinguish whether a particular frequency shift is caused by a perturbation below or beyond the EP, complicating the system's use as a reliable threshold sensor. Essentially, the system is unable to provide a directional response, i.e., to respond only when the perturbation exceeds a certain threshold value, because perturbations on either side of the EP would produce a similar spectral shift. A concrete example (a PT-symmetric electrical circuit based on a sixth-order EP) is provided in Sec. III.

It is worth emphasizing that, for a system designed to function as a threshold sensor, it is critical that the structure is injective, meaning that the response is monotonic and distinct in one direction only, either for perturbations above or below the threshold. An EP-based sensor intended to function as a sensory threshold should have a structure where the response is confined to one branch, ensuring that only perturbations above (or below) the EP elicit a detectable output. In a non-injective structure, this condition is not met, and the sensor becomes unsuitable for threshold applications.

C. Stochastic resonance

Stochastic resonance is a fundamental phenomenon in nonlinear and statistical physics [85, 88–90], where an optimal level of noise can have a beneficial role in enhancing the system's response to weak inputs. Recently, stochastic processes in EP-based structures were investigated in [27], opening the door to innovative sensor designs capable of exploiting the inherent noise of the system to

achieve improved performance with implications across diverse application domains.

In the theory of stochastic processes, the EPs in certain structures exhibit a unique capacity: they can operate as dynamic sensory thresholds, generating random frequency shifts when subject to a time-varying input. In these systems, EPs play a role in separating two distinct phases of the system response, one which is insensitive to the input ($\mathrm{Re}\{\delta\omega\} = 0$) and another that is sensitive $\mathrm{Re}\{\delta\omega\} > 0$. Further, the system is able to exploit the fluctuations induced by noise to its advantage, thereby enhancing its sensitivity to weak input variations, a stochastic-resonance like phenomenon. To quantify a stochastic resonance in a system with an EP, we analyze whether the additional noise paradoxically increases the sensor's SNR. Our aim is to demonstrate that a stochastic resonance around the EPs (stochastic EPs) can be exploited for developing sensors capable of functioning effectively under environmental fluctuations.

It is worth noting that the primary difference between a second-order EP and a higher order EP lies in their sensitivity to perturbations. For the latter, such as a third-order EP, the system's sensitivity can increase significantly compared to a second-order EP. This sensitivity can be quantified by the relationship $\epsilon^{1/(n-1)}$, where n denotes the order of the EP. Consequently, a system operating at a third-order EP is more sensitive to noise than one at a second-order EP, meaning that even smaller perturbations can induce a larger response. Practically, this enhanced sensitivity can lead to a steeper initial rise in the SNR as the noise amplitude (σ) increases, because the system is more responsive to stochastic fluctuations. However, due to this heightened sensitivity, a higher-order EP system reaches the critical noise level sooner, beyond which the SNR begins to decrease. This contrasts with a second-order EP, where the system is less sensitive to perturbation, causing the critical noise level to occur at a higher amplitude. Overall, while both second-order and higher-order EPs show an increase in the SNR with noise up to a critical value followed by a decline, a system with a higher-order EP may reach its peak SNR earlier and is more sensitive to small noise perturbations.

To offer a more comprehensive understanding of the three EP structures, we study each within the context of electrical sensors through case studies.

III. STOCHASTIC RESONANCE IN SYSTEMS WITH HIGH-ORDER EXCEPTIONAL POINTS

Our prototypical system consists of three inductively coupled resonators as a wireless sensor [26], which are described by a pseudo-Hermitian effective matrix, as shown in Fig. 5(a). The sensor can be designed to exhibit a high-order EP in both branch and monotonic structures, thereby capable of operating as a dynamic sensory threshold. The system equations can be derived by a standard circuit analysis. In particular, the three inductors are coupled through electromagnetic induction in which the voltages V_{L_n} and currents I_n flowing through the inductors are related to each other as

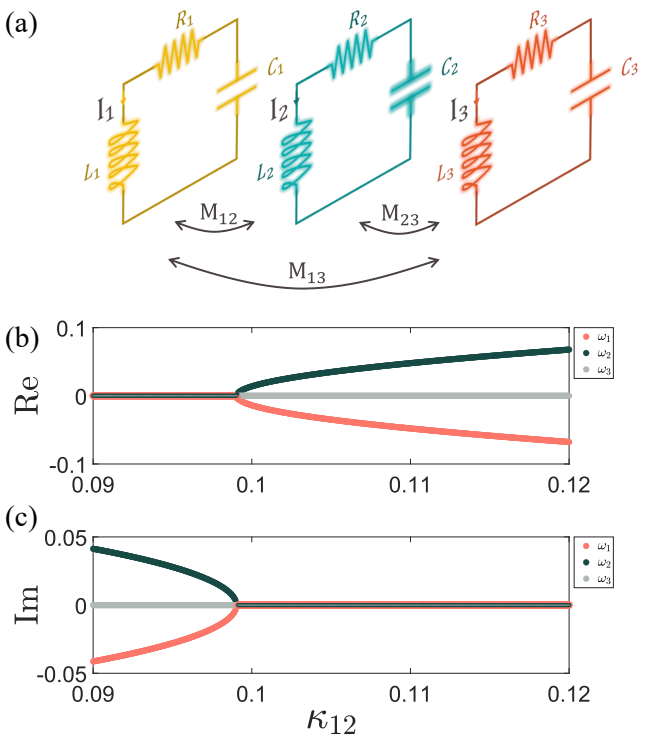

FIG. 5. System of three inductively coupled resonators as a wireless sensor. (a) A schematic illustration of the circuit system. (b,c) Real and imaginary parts of the eigenfrequency of the system (3) as a function of mutual coupling parameter κ_{12}, respectively. Other parameter values are $\alpha = 50$, $\gamma = 0.1$, $\kappa_{13} = 0$, and $\kappa_{23} = (1+\alpha)^{3/2}\kappa_{12}$. The response of the three coupled RLC resonators exhibits a branch structure: for $\kappa_{12} < \kappa_{EP}$, the perturbed system has one real eigenfrequency ($\omega_3 = 0$) and two complex conjugate eigenfrequencies, whereas for $\kappa_{12} > \kappa_{EP}$, it has three distinct real eigenfrequencies.

$$\begin{bmatrix} V_{L_1} \\ V_{L_2} \\ V_{L_3} \end{bmatrix} = i\omega \begin{bmatrix} L_1 & M_{12} & M_{13} \\ M_{12} & L_2 & M_{23} \\ M_{13} & M_{23} & L_3 \end{bmatrix} \begin{bmatrix} I_1 \\ I_2 \\ I_3 \end{bmatrix}, \tag{1}$$

where L_n are the inductances and M_{nk} $(n, k = 1, 2, 3)$ is the mutual inductance. Applying the Kirchhoff voltage law, we have

$$i\omega I_1 + i\omega \tfrac{M_{12}}{L_1} I_2 + i\omega \tfrac{M_{13}}{L_1} I_3 + \tfrac{R_1}{L_1} I_1 + \tfrac{1}{ic_1 L_1 \omega} I_1 = 0, \tag{2a}$$

$$i\omega \tfrac{M_{12}}{L_2} I_1 + i\omega I_2 + i\omega \tfrac{M_{23}}{L_2} I_3 + \tfrac{R_2}{L_2} I_2 + \tfrac{1}{ic_2 L_2 \omega} I_2 = 0, \tag{2b}$$

$$i\omega \tfrac{M_{13}}{L_3} I_1 + i\omega \tfrac{M_{23}}{L_3} I_2 + i\omega I_3 + \tfrac{R_3}{L_3} I_3 + \tfrac{1}{ic_3 L_3 \omega} I_3 = 0. \tag{2c}$$

These equations can be recast into a Schrödinger-type of equation:

$$i\dot{I} = HI, \tag{3a}$$

$$H = \begin{bmatrix} -i\frac{R_1}{L_1} - \frac{1}{C_1 L_1 \omega} & \frac{M_{12}}{L_1}\omega & \frac{M_{13}}{L_1}\omega \\ \frac{M_{12}}{L_2}\omega & -i\frac{R_2}{L_2} - \frac{1}{C_2 L_2 \omega} & \frac{M_{23}}{L_2} \\ \frac{M_{13}}{L_3}\omega & \frac{M_{23}}{L_3} & -i\frac{R_3}{L_3} - \frac{1}{C_3 L_3 \omega} \end{bmatrix}, \quad (3b)$$

where $I = (I_1, I_2, I_3)^T$ are the system variables and H is the effective Hamiltonian operator. The simplified approximation of Eq. (3) can be obtained by assuming $\omega \approx \omega_0$ and defining the resonant frequencies as $\omega_0 = 1/\sqrt{C_n L_n}$ with $L_n = L$ and $C_n = C$. The gain/loss parameter is $\gamma_n = R_n\sqrt{C/L}$ and the inductive coupling coefficient is $\kappa_{nk} = M_{nk}/L$. The effective Hamiltonian is then reduced to $H = \omega_0(\tilde{H} - \mathbb{I})$:

$$\tilde{H} = \begin{bmatrix} -i\gamma_1 & \kappa_{12} & \kappa_{13} \\ \kappa_{12} & -i\gamma_2 & \kappa_{23} \\ \kappa_{13} & \kappa_{23} & -i\gamma_3 \end{bmatrix}, \quad (4)$$

where $\mathbb{I}$ is a 3×3 identity matrix. Using the substitution $\tilde{\omega} = 1 + \omega/\omega_0$, we can calculate the eigenfrequencies through the associated characteristic equation $\det\left(\tilde{H} - \tilde{\omega}\mathbb{I}\right) = 0$:

$$\begin{aligned} &\tilde{\omega}^3 + i\left(\gamma_1 + \gamma_2 + \gamma_3\right)\tilde{\omega}^2 \\ &- \left(\kappa_{12}^2 + \kappa_{13}^2 + \kappa_{23}^2 + \gamma_1\gamma_2 + \gamma_1\gamma_3 + \gamma_2\gamma_3\right)\tilde{\omega} \\ &- \left(2\kappa_{12}\kappa_{13}\kappa_{23} + i\left(\gamma_1\gamma_2\gamma_3 + \gamma_1\kappa_{23}^2 + \gamma_2\kappa_{13}^2 + \gamma_3\kappa_{12}^2\right)\right) = 0. \end{aligned} \quad (5)$$

The real and imaginary parts of the characteristic equation are, respectively,

$$\begin{aligned} &\tilde{\omega}^3 - \left(\kappa_{12}^2 + \kappa_{13}^2 + \kappa_{23}^2 + \gamma_1\gamma_2 + \gamma_1\gamma_3 + \gamma_2\gamma_3\right)\tilde{\omega} \\ &\quad - \left(2\kappa_{12}\kappa_{13}\kappa_{23}\right) = 0, \end{aligned} \quad (6)$$

and

$$\begin{aligned} &\left(\gamma_1 + \gamma_2 + \gamma_3\right)\tilde{\omega}^2 \\ &- \left(\gamma_1\gamma_2\gamma_3 + \gamma_1\kappa_{23}^2 + \gamma_2\kappa_{13}^2 + \gamma_3\kappa_{12}^2\right) = 0. \end{aligned} \quad (7)$$

From the characteristic equation, we can then determine the conditions for the system to be pseudo-Hermitian and the conditions under which a third-order EP can emerge.

Pseudo-Hermiticity. A system whose Hamiltonian can be related to its adjoint through a similarity transformation is a pseudo-Hermitian system satisfying

$$\det\left(\tilde{H} - \tilde{\omega}I\right) = \det\left(\tilde{H}^\dagger - \tilde{\omega}I\right).$$

For a symmetric Hamiltonian, this condition can be simplified to

$$\det\left(\tilde{H} - \tilde{\omega}I\right) = \det\left(\tilde{H}^* - \tilde{\omega}I\right)$$

or

$$\mathrm{Im}\{\det\left(\tilde{H} - \tilde{\omega}I\right)\} = 0,$$

which is Eq. (7) with the following conditions:

$$\gamma_1\gamma_2\gamma_3 + \gamma_1\kappa_{23}^2 + \gamma_2\kappa_{13}^2 + \gamma_3\kappa_{12}^2 = 0, \quad (8a)$$

$$\gamma_1 + \gamma_2 + \gamma_3 = 0, \quad (8b)$$

where the condition (8b) stipulates a balance between the total gain and loss of the system. We consider the first resonator's gain $\gamma_1 = -g$ and the other resonator's losses $\gamma_2 = \alpha\gamma_3$, leading to

$$\gamma_2 = \frac{\alpha g}{1+\alpha},$$
$$\gamma_3 = \frac{g}{1+\alpha}.$$

Exceptional point. From Eq. (6), we see that a third-order EP arises when the following conditions are met:

$$\kappa_{12}^2 + \kappa_{13}^2 + \kappa_{23}^2 + \gamma_1\gamma_2 + \gamma_1\gamma_3 + \gamma_2\gamma_3 = 0, \quad (9a)$$

$$2\kappa_{12}\kappa_{13}\kappa_{23} = 0, \quad (9b)$$

where the condition (9b) can be satisfied only if one of the coupling coefficients is zero. For $\kappa_{13} = 0$, we can solve Eqs. (8a) and (9a) to obtain

$$\kappa_{12} = g\sqrt{\frac{1+\alpha}{2+\alpha}},\ \kappa_{23} = \frac{g}{(1+\alpha)\sqrt{2+\alpha)}}. \quad (10)$$

The last possible case is $\kappa_{23} = 0$. In this case, Eqs. (8a) and (9a) do not have a solution.

In Ref. [78], the constraints needed for the emergence of EPs in the presence of symmetries were described, where an nth-order EP can emerge when $2(n-1)$ real constraints are satisfied. Our goal is to study the emergence of higher-order EPs within the context of pseudo-Hermitian systems. To generate a stable nth-order EP, both the pseudo-Hermiticity and EP conditions need to be satisfied, where n eigenvalues and their corresponding eigenstates coalesce. For example, Eqs. (8a) and (8b) define the pseudo-Hermiticity condition, while Eqs. (9a) and (9b) ensure the existence of a third-order EP. Altogether, four constraints need to be satisfied, which is consistent with the previous result [78].

In general, the feasibility of realizing higher-order EPs in one-dimensional space depends on the realization of the pseudo-Hermitian matrix. It is necessary that the conditions for both pseudo-Hermiticity and EP be satisfied. For instance, the condition in Eq. (9b) can only be satisfied if one of the coupling coefficients is zero. Yet, for $\kappa_{23} = 0$, the system becomes infeasible, as Eqs. (8a) and (9a) no longer have a solution. This illustrates the delicate balance needed to generate a higher-order EP in practical systems.

In the following, we study two distinct physical perturbation scenarios, each with its potential applications in threshold sensing, and present a circuit system with a non-injective structure that is not suitable for threshold sensing.

A. Mutual coupling κ_{12} as a perturbation

For $\kappa_{13} = 0$, Eq. (6) leads to three eigenfrequencies that evolve smoothly as a function of the perturbation κ_{12}. Figures 5(b) and 5(c) show the real and imaginary parts of the eigenfrequency, respectively. It can be seen that, when κ_{12} is perturbed, the response of the three coupled RLC resonators has a branch structure. Before the EP, $\mathrm{Re}\{\delta\omega\} = 0$ and the system is insensitive to the input. At the bifurcation point κ_{EP}, all eigenfrequencies and their corresponding eigenvectors coalesce, and a small added perturbation can abruptly induce a frequency shift and result in a strongly nonlinear response. Now consider a time-varying inductive coupling parameter $\kappa_{12}(t)$, where the input signal can be decomposed as $\kappa_{12}(t) = \kappa_b + \kappa_s sin(\nu t)$ with κ_b the dc part of the coupling strength, κ_s the amplitude of the oscillatory part, and ν the angular frequency. To investigate stochastic resonance in such a structure, we consider white noise with standard deviation σ added to the time-varying coupling $\kappa_{12}(t)$, where $\kappa_b + \kappa_s \leq \kappa_{EP}$. For $\kappa_{12}(t) \leq \kappa_{EP}$, a stochastic EP arises as a sensory threshold, resulting in an intermittent output of random frequency shift, as shown in Fig. 6(d), with a spectral peak at the signal angular frequency ν.

The effect of the stochastic EP can be quantified by the SNR of the output, which is the ratio of the signal power to the background noise power. To calculate the SNR statistically, we need the power spectral density - the Fourier transform of the autocorrelation function of the output. The power of the signal is proportional to the peak height of the power spectrum at the frequency of the time-varying input. Since all the spectrum other than the peaks is the background noise, the power of the noise is the sum of the rest of the spectral densities at the other frequencies. Figure 6(e) shows that the SNR of the system has a broad peak in $\sigma_c > 0$. Initially, as σ increases from zero, the SNR rapidly increases, suggesting that the noise paradoxically enhances the performance of the sensor. This observation holds up to an optimal level of the noise σ_c, where the SNR gradually decreases beyond this point. This result indicates that stochastic high-order EP not only amplifies the sensitivity to perturbations but also contributes to an overall improvement in the system performance, which is characteristic of a stochastic resonance. The remarkable feature is that the SNR initially increases rapidly with the noise amplitude and, after reaching the maximum at an optimal noise level, the SNR decreases slowly. This gives rise to a wider range of the noise amplitude around the optimal noise to achieve a relatively large SNR. The phenomenon can be exploited for practical applications of sensors such as wearable sensors in which a stochastic EP arising from physiological motion overcomes the negative effect of noise, resulting in more accurate tracking of a person's vital signs [27].

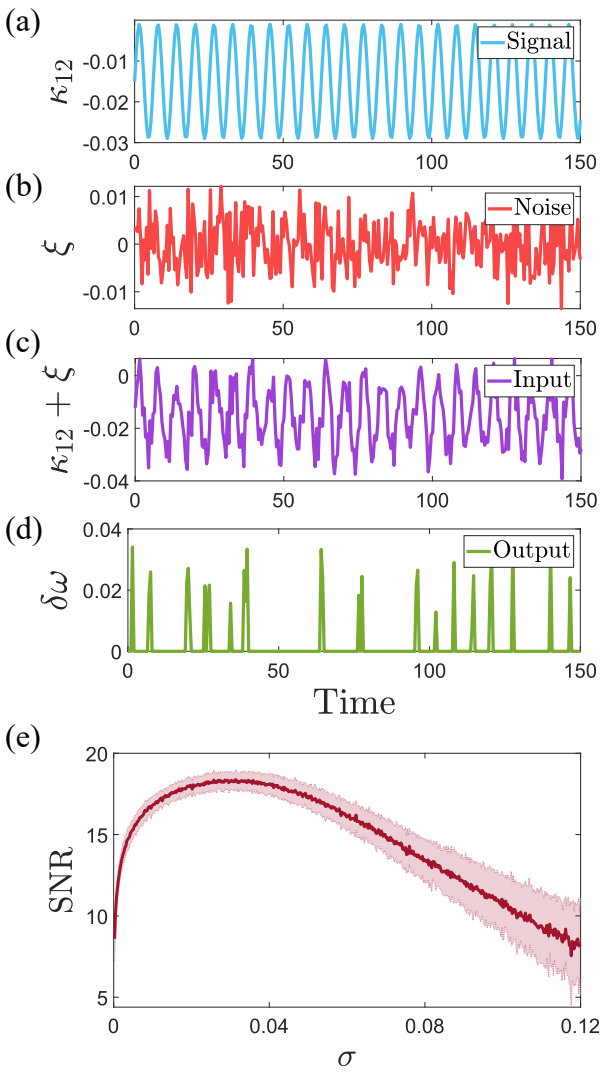

FIG. 6. Emergence of a stochastic resonance through a stochastic EP as a sensory threshold. (a) Input sinusoidal signal $\kappa_{12}(t)$ of amplitude $\kappa_b + \kappa_s = 0.099$. (b) Gaussian white noise of amplitude $\sigma = 0.03$. (c) The noisy input signal. (d) Output of the system, a sequence of the pulses that appear randomly in time. (e) SNR as a function of the noise amplitude σ. This smooth and broad SNR curve is obtained by averaging 1000 independent realizations of the process and the shaded area indicates the standard deviation. Other parameter values are $\alpha = 50$, $\gamma = 0.1$, and $\kappa_{13} = 0$.

B. Capacitive Perturbation ε

Consider a capacitive perturbation ε applied to the relay resonator at EP, where $\kappa_{13} = 0$, κ_{12} and κ_{23} take on values as in Eq. (10). The characteristic equation of the perturbed system is

$$\det\left(\hat{H} - \varepsilon H_e - \hat{\omega}\mathbb{I}\right) = 0,$$

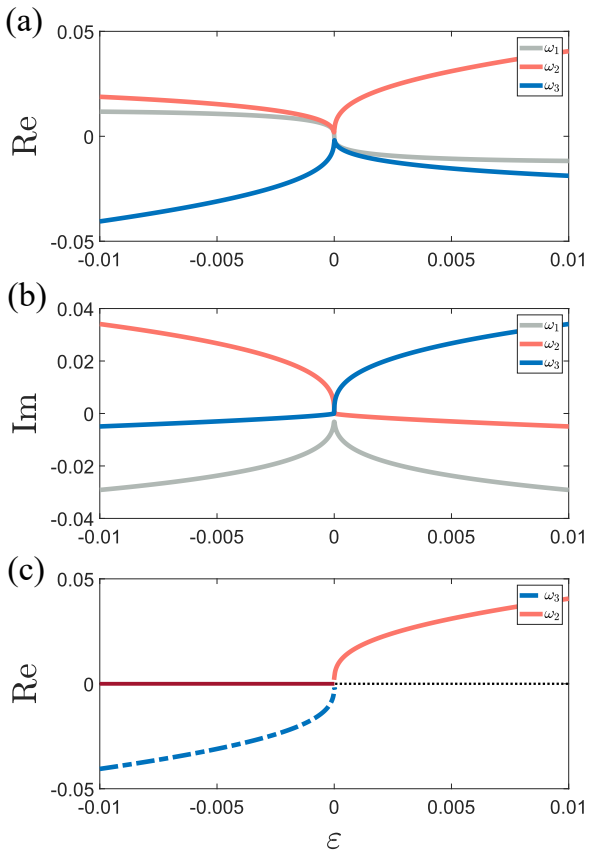

FIG. 7. Effect of a capacitive perturbation on the EP dynamics. Shown are the (a) real and (b) imaginary parts of the eigenfrequency evolution of the system (3) as a function of the perturbation ε for $\alpha = 1$, $\gamma = 0.1$, $\kappa_{13} = 0$, and $\kappa_{23} = (1+\alpha)^{3/2}\kappa_{12}$. (c) Reflection spectrum of the system in response to a capacitive perturbation. Shown is the eigenfrequency shift in response to the perturbation ε.

where H_e is a 3×3 matrix that has one nonzero element on the second entry of the main diagonal. We have

$$\hat{\omega}^3 - \varepsilon\hat{\omega}^2 + i\varepsilon\frac{\alpha g}{1+\alpha}\hat{\omega} - \varepsilon\frac{g^2}{1+\alpha} = 0. \tag{11}$$

Fixing $\alpha = 1$ and $g = 0.1$, the real and the imaginary parts of the eigenfrequency can be obtained by solving Eq. (11), as shown in Fig. 7(a) and 7(b), respectively. It can be seen that any small perturbation applied to the EP (the bifurcation point of the system) gives rise to three different complex numbers, among which only one has physical significance: the eigenfrequency associated with a higher spectral resolution, in close relation to having a higher Q factor or a narrower linewidth splitting $\mathrm{Im}\{\delta\omega\}$. This suggests the eigenfrequency with the smallest magnitude of the imaginary part as the feasible choice for sensing applications, corresponding to the green curve $\hat{\omega}_1$ for $\varepsilon < 0$ and the red curve $\hat{\omega}_2$ for $\varepsilon > 0$ in Fig. 7. The eigenfrequency shift in response to the perturbation ε at EP exhibits a monotonic pattern, where the response of the system corresponding to one side of EP can selectively be filtered out, e.g., the green dot-dashed part of the response in Fig. 7(c). In this case, the system has a saddle point ε_{EP}. The system's response to perturbations smaller than EP is unresponsive to the input (it is filtered out) and a small perturbation larger than EP can abruptly induce a frequency shift leading to a highly nonlinear response.

We now study the case where the input signal is the time-varying coupling parameter: $\varepsilon(t) = \varepsilon_b + \varepsilon_s \sin(\nu t)$, where ε_b is the dc part of the coupling strength, ε_s the amplitude of the oscillatory part, and ν is the angular frequency, and $\varepsilon_b + \varepsilon_s \leq \varepsilon_{EP}$, as shown in Fig. 8(a). To induce a stochastic resonance, we add Gaussian white noise of amplitude σ, as shown in Fig. 8(b), to $\varepsilon(t)$. The resulting noisy input signal is shown in Fig. 8(c), where $\varepsilon(t) \leq \varepsilon_{EP}$. The output of the system is intermittent, as shown in Fig. 8(d), corresponding to a random frequency shift with a spectral peak at the signal angular frequency ν. Figure 8(e) shows the the SNR of the system versus the noise amplitude. The SNR first rises quickly with the noise, reaches a maximum at the optimal noise amplitude σ_c, and then decreases slowly afterwards. This is indicative of a stochastic resonance in the presence of a stochastic high-order EP, signifying an enhancement in the system's performance assisted by noise in a wide range.

C. A PT-symmetric electrical circuit

We consider a PT-symmetric electrical circuit based on a sixth-order EP, which is composed of two LC resonators parallel with a resistor coupled with a grounded capacitor C_0, as shown in Fig 9(a). Using the current Kirchhoff's law with normalization $\tau = \omega_0 t$, we have that the resonant frequency is $\omega_0 = 1/\sqrt{LC}$, the intrinsic loss or gain rate of the LC resonator is $\gamma = R\sqrt{C/L}$, and the coupling coefficient between the two resonators is $\mu = C/C_0$. The voltages at various nodes of the circuit can be recast into the Schrödinger-type equation as:

$$i\dot{\Phi} = H\Phi, \tag{12a}$$

$$H = i\begin{pmatrix} 0 & 0 & 0 & 1 & 0 & 0 \\ 0 & 0 & 0 & 0 & 1 & 0 \\ 0 & 0 & 0 & 0 & 0 & 1 \\ -1 & 1 & 0 & -\gamma & 0 & 0 \\ \mu & -2\mu & \mu & 0 & 0 & 0 \\ 0 & 1 & -1 & 0 & 0 & \gamma \end{pmatrix}. \tag{12b}$$

The eigenfrequencies can be found through the associated characteristic equation $\det(H - \omega\mathbb{I}) = 0$:

$$\omega^2[\omega^4 + (\gamma^2 - 2 - 2\mu)\,\omega^2 + 1 + 2\mu - 2\mu\gamma^2] = 0, \tag{13}$$

where $\mathbb{I}$ is the 6×6 unity matrix. Solving Eq. (13) leads to six eigenfrequencies as:

$$\omega^*_{1,2} = 0,$$
$$\omega^*_{3-6} = \pm\frac{1}{\sqrt{2}}\sqrt{2 + 2\mu - \gamma^2 \pm \sqrt{\gamma^4 + (4\mu - 4)\gamma^2 + 4\mu^2}}. \tag{14}$$

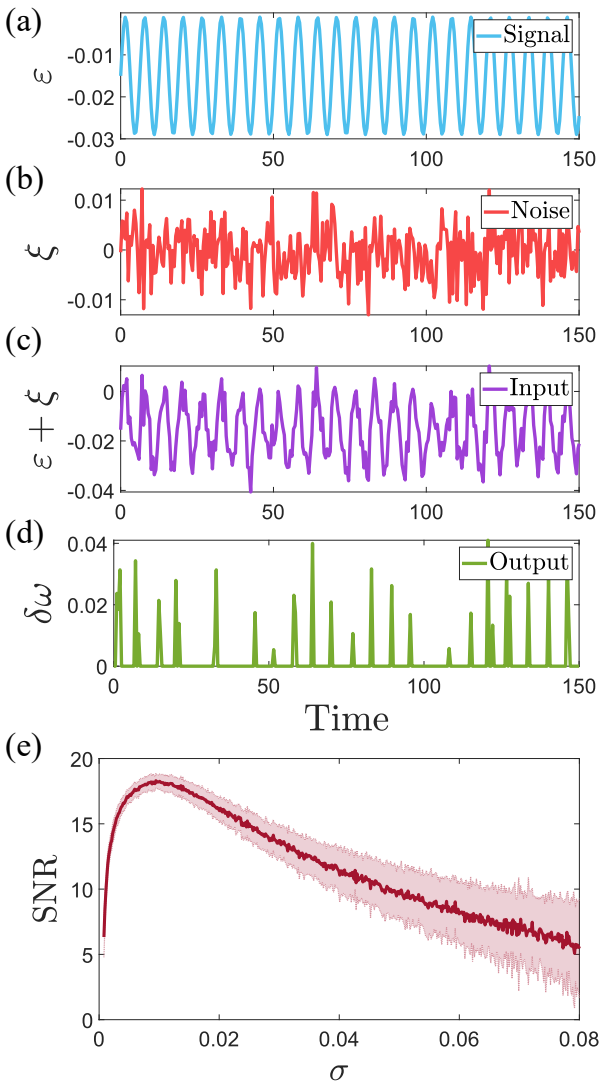

FIG. 8. Emergence of a stochastic resonance with a capacitive perturbation, where a stochastic EP functions as a sensory threshold. The system is described by Eq. (3). (a) A time-varying sinusoidal input signal $\varepsilon(t)$ of the amplitude $\varepsilon = -0.01$. (b) Gaussian white noise of amplitude $\sigma = 0.03$. (c) The noise input signal. (d) The output signal - a sequence of random pulses. (e) SNR versus the noise amplitude, which is indicative of a stochastic resonance. Similar to the resonance behavior in Fig. 6(e), the SNR initially rises quickly with the noise amplitude and then decreases slowly after reaching a maximum, giving rise to a relatively wide interval of the noise amplitude for achieving a large SNR. Other parameter values are $\alpha = 1$, $\gamma = 0.1$, and $\kappa_{13} = 0$.

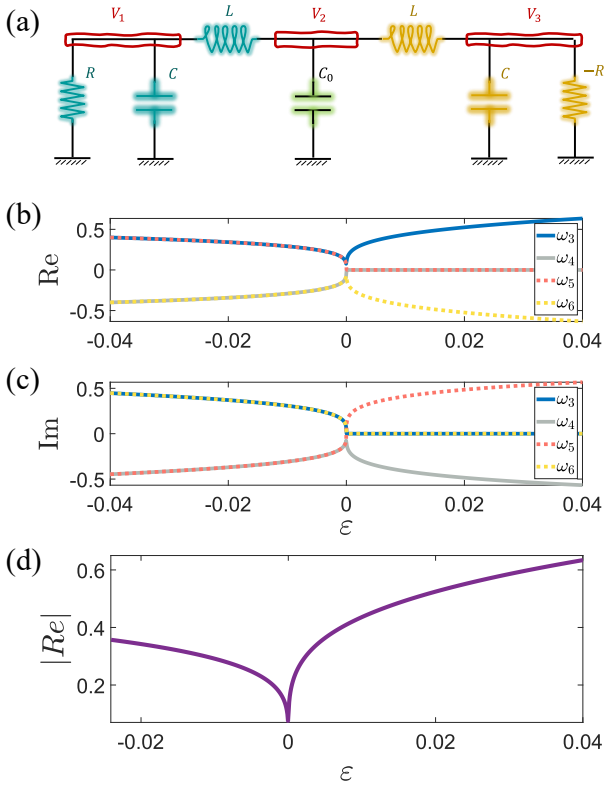

FIG. 9. A PT-symmetric sensing resonator with the negative impedance that can be realized with an operational amplifier. The system is described by Eq. (12). (a) The circuit diagram. (b,c) Real and imaginary parts of eigenfrequency as a function of perturbation ε to the parameter μ. (d) Eigenfrequency shift in response to the perturbation ε. Other parameters are $\mu_0 = (-1 + \sqrt{5})/4$ and $\gamma = (1 + \sqrt{5})/2$.

Figures 9(b) and 9(c) show ω^*_{3-6} versus the perturbation ε to the parameter μ. It can be seen that the high-order EP at $\omega^* = 0$ holds for $\gamma_{EP} = (1 + \sqrt{5})/2$ and $\mu_{EP} = (-1 + \sqrt{5})/4$. For perturbation $\varepsilon < \varepsilon_{EP}$, all the eigenfrequencies share the same absolute imaginary parts ($\mathrm{Im}\{\omega\}$) with different real parts, resulting in the eigenfrequency shifts both to the right and to the left associated with the reflection coefficient of the system. For $\varepsilon > \varepsilon_{EP}$, the eigenfrequencies corresponding to the smallest $\mathrm{Im}\{\omega\}$ are highlighted in yellow and green, which share the same absolute real parts. This implies that the reflection coefficient of the system has eigenfrequency shift both to the right and to the left. Consequently, the response of the system to perturbation corresponding to the smallest $\mathrm{Im}\{\omega\}$ belongs to that of a non-injective structure with a bifurcation point at ε_{EP}. Figure 9(d) shows the absolute values of the frequency shift with respect to the applied perturbation. Due to the symmetric nature of the system's response, the sensor illustrated in Fig. 9 is not a suitable choice for sensory threshold applications. Instead, a potential application lies in enhancing the system's sensory response rather

than serving as a sensory threshold. A key factor is that the system's response to perturbations, whether they are of higher or smaller values than the EP, cannot be reliably distinguished [25].

In this example of a PT-symmetric electrical circuit, there is a symmetric response to perturbations. Regardless of whether the perturbation is above or below the EP, the eigenfrequency shifts to the right or the left, depending on the reflection coefficient of the system. Due to this symmetry, the sensor presented in Fig. 9 cannot serve as a threshold sensor because it lacks the ability to distinguish between higher and lower perturbations. Instead, such systems are more suited for applications where enhancing overall sensitivity is the goal, rather than serving as a threshold sensor.

IV. DISCUSSION

We have investigated the possibility of exploiting pseudo-Hermitian systems for sensing applications, focusing on the dynamics about a high-order EP. The frequency response of the sensory system with a high-order EP to perturbations can be categorized into three scenarios: branch, monotonic, and non-injective. In each case, the splitting in the real part of the frequency reveals EPs as a critical point around which the system exhibits enhanced sensitivity to perturbations. A high-order EP can enhance sensitivity, rendering it desired for sensory threshold applications, where the system can leverage the presence of noise to improve its performance. We have demonstrated that the interplay among the exceptional point, perturbation as input signal, and noise leads to a stochastic resonance. This stochastic resonance associated with a high-order EP has one appealing feature. As indicated in Figs. 6(e) and 8(e) for two distinct types of perturbations (input signals), the SNR versus the noise amplitude exhibits a broad maximum. This means that a precise tuning of the noise amplitude is not required, as there exists a range of the amplitude in which the SNR maintains at a high value. The phenomenon of high-order EP induced stochastic resonance not only underscores the practical applicability but also extends the boundaries of potential applications in signal processing and sensor technology.

The energy or frequency splitting at an EP follows an exponential relationship with the strength of the perturbation, expressed as $\epsilon^{1/(n-1)}$, where n is the order of the EP. This relation implies a significantly higher sensitivity compared to that associated with a diabolic point found in conventional sensors. In our work, we extended this sensitivity to scenarios where the input signal is weak and typically set at or below the sensory threshold. Under such conditions, without noise, no detectable output would be expected. However, due to the system's extreme sensitivity at the EP, even the intrinsic noise of the system can act as a perturbation, enabling the detection of an output. The SNR values depicted in Figs. 6 and 8 reflect this phenomenon, demonstrating that there exists an optimal noise strength where the SNR is maximized. This outcome is directly related to the exponential sensitivity of the EP to perturbations, including noise. At low noise levels, the input signal remains undetectable, while at higher noise levels, the system becomes overwhelmed by noise. As a result, there is an optimal noise strength that enhances the SNR by leveraging the EP's sensitivity to weak perturbations. For a fair comparison, the original SNR value without any noise or perturbations can be considered as a baseline value, where the system would exhibit no detectable signal in the output due to the input signal being below the threshold. The results in Figs. 6 and 8 thus demonstrate how the introduction of noise allows the system to surpass this baseline and exhibit enhanced detection capability.

It is worth noting that the extended (monotonic) structure is particularly appealing for real-world sensing applications. It can arise in systems with PT or pseudo-Hermitian symmetry, where broader experimental platforms are available compared with the branch-type of structures. For example, in an optomechanical accelerometer [28] consisting of a pair of Fabry-Péot multilayer cavities with loss and gain cavity, respectively, a PT symmetric system with a second-order EP can be constructed on a silicon platform. In this system, the positive (negative) acceleration results in the right (left) hand shift direction in spectra, which is exactly what the monotonic structure exhibits. For pseudo-Hermitian systems with a third-order EP [29] in cavity optomechanics, the eigenvalue spectrum versus the detuning disturbance displays the extended structure since only the zero imaginary part can be distinguished and observed in the experiment. As a result, with the monotonic structure, capacity as disturbance can then be applied to an accelerometer for a wide range of applications [28, 91–93], including navigation devices, gravity gradiometry, earthquake monitoring [94, 95], airbag deployment sensors in automobiles, and consumer electronics protection. In addition, the capacity can also be designed as a hypersensitive microfluid speed sensor (temperature sensor) [25, 96] and pressure sensor [56, 97].

ACKNOWLEDGMENTS

This work was supported by the Air Force Office of Scientific Research under Grant No. FA9550-21-1-0438 and by the Office of Naval Research under Grant No. N00014-24-1-2548.

[1] H. Cao and J. Wiersig, Dielectric microcavities: Model systems for wave chaos and non-Hermitian physics, Rev. Mod. Phys. **87**, 61 (2015).

[2] L. Huang, H.-Y. Xu, C. Grebogi, and Y.-C. Lai, Relativistic quantum chaos, Phys. Rep. **753**, 1 (2018).

[3] R. El-Ganainy, K. G. Makris, M. Khajavikhan, Z. H. Musslimani, S. Rotter, and D. N. Christodoulides, Non-Hermitian physics and PT symmetry, Nat. Phys. **14**, 11 (2018).

[4] K. Kawabata, K. Shiozaki, M. Ueda, and M. Sato, Symmetry and topology in non-Hermitian physics, Phys. Rev. X **9**, 041015 (2019).

[5] E. Lee, H. Lee, and B.-J. Yang, Many-body approach to non-Hermitian physics in fermionic systems, Phys. Rev. B **101**, 121109 (2020).

[6] S. Franca, V. Könye, F. Hassler, J. van den Brink, and C. Fulga, Non-Hermitian physics without gain or loss: the skin effect of reflected waves, Phys. Rev. Lett. **129**, 086601 (2022).

[7] R. Yang, L. Huang, Y.-C. Lai, and C. Grebogi, Quantum chaotic scattering in graphene systems, EPL **94**, 40004 (2011).

[8] L. Huang, R. Yang, and Y.-C. Lai, Geometry-dependent conductance oscillations in graphene quantum dots, EPL **94**, 58003 (2011).

[9] R. Yang, L. Huang, Y.-C. Lai, and L. M. Pecora, Modulating quantum transport by transient chaos, Appl. Phys. Lett. **100**, 093105 (2012).

[10] X. Ni, L. Huang, Y.-C. Lai, and L. M. Pecora, Effect of chaos on relativistic quantum tunneling, EPL **98**, 50007 (2012).

[11] L. Ying, L. Huang, Y.-C. Lai, and C. Grebogi, Conductance fluctuations in graphene systems: The relevance of classical dynamics, Phys. Rev. B **85**, 245448 (2012).

[12] G.-L. Wang, L. Ying, Y.-C. Lai, and C. Grebogi, Quantum chaotic scattering in graphene systems in the absence of invariant classical dynamics, Phys. Rev. E **87**, 052908 (2013).

[13] X. Ni, L. Huang, L. Ying, and Y.-C. Lai, Relativistic quantum tunneling of a dirac fermion in nonhyperbolic chaotic systems, Phys. Rev. B **87**, 224304 (2013).

[14] L. Ying, G. Wang, L. Huang, and Y.-C. Lai, Quantum chaotic tunneling in graphene systems with electron-electron interactions, Phys. Rev. B **90**, 224301 (2014).

[15] W. Pauli, On Dirac's new method of field quantization, Rev. Mod. Phys. **15**, 175 (1943).

[16] A. Mostafazadeh, Pseudo-Hermiticity versus PT symmetry: the necessary condition for the reality of the spectrum of a non-Hermitian Hamiltonian, J. Math. Phys. **43**, 205 (2002).

[17] A. Mostafazadeh, Pseudo-Hermiticity versus PT-symmetry. II. A complete characterization of non-Hermitian Hamiltonians with a real spectrum, J. Math. Phys. **43**, 2814 (2002).

[18] A. Mostafazadeh, Pseudo-Hermiticity versus PT-symmetry III: Equivalence of pseudo-Hermiticity and the presence of antilinear symmetries, J. Math. Phys. **43**, 3944 (2002).

[19] G. Lindblad, On the generators of quantum dynamical semigroups, Commun. Math. Phys. **48**, 119 (1976).

[20] V. Gorini, A. Kossakowski, and E. C. G. Sudarshan, Completely positive dynamical semigroups of n-level systems, J. Math. Phys. **17**, 821 (1976).

[21] G. Gamow, Zur quantentheorie des atomkernes, Z. Physik **51**, 204 (1928).

[22] K. Kawano and T. Kitoh, *Introduction to Optical Waveguide Analysis: Solving Maxwell's Equation and the Schrödinger Equation* (John Wiley & Sons, 2004).

[23] M. Guidry, Y. Song, C. Lafargue, R. Sobczyk, D. Decanini, S. Bittner, B. Dietz, L. Huang, J. Zyss, A. Grigis, *et al.*, Three-dimensional micro-billiard lasers: the square pyramid, EPL **126**, 64004 (2019).

[24] Y. N. Joglekar and S. J. Wolf, The elusive memristor: properties of basic electrical circuits, Eur. J. Phys. **30**, 661 (2009).

[25] Z. Xiao, H. Li, T. Kottos, and A. Alù, Enhanced sensing and nondegraded thermal noise performance based on PT-symmetric electronic circuits with a sixth-order exceptional point, Phys. Rev. Lett. **123**, 213901 (2019).

[26] K. Yin, X. Hao, Y. Huang, J. Zou, X. Ma, and T. Dong, High-order exceptional points in pseudo-Hermitian radio-frequency circuits, Phys. Rev. Appl. **20**, L021003 (2023).

[27] Z. Li, C. Li, Z. Xiong, G. Xu, Y. R. Wang, X. Tian, X. Yang, Z. Liu, Q. Zeng, R. Lin, Y. Li, J. K. W. Lee, J. S. Ho, and C.-W. Qiu, Stochastic exceptional points for noise-assisted sensing, Phys. Rev. Lett. **130**, 227201 (2023).

[28] R. Kononchuk and T. Kottos, Orientation-sensed optomechanical accelerometers based on exceptional points, Phys. Rev. Res. **2**, 023252 (2020).

[29] W. Xiong, Z. Li, Y. Song, J. Chen, G.-Q. Zhang, and M. Wang, Higher-order exceptional point in a pseudo-Hermitian cavity optomechanical system, Phys. Rev. A **104**, 063508 (2021).

[30] W. Heiss, The physics of exceptional points, J. Phys. A Math. Theor. **45**, 444016 (2012).

[31] T. Kato, *Perturbation Theory for Linear Operators*, Vol. 132 (Springer Science & Business Media, 2013).

[32] M.-A. Miri and A. Alu, Exceptional points in optics and photonics, Science **363**, eaar7709 (2019).

[33] H. Hodaei, A. U. Hassan, S. Wittek, H. Garcia-Gracia, R. El-Ganainy, D. N. Christodoulides, and M. Khajavikhan, Enhanced sensitivity at higher-order exceptional points, Nature **548**, 187 (2017).

[34] H. Zhao, Z. Chen, R. Zhao, and L. Feng, Exceptional point engineered glass slide for microscopic thermal mapping, Nat. Commun. **9**, 1764 (2018).

[35] R. Kononchuk, J. Cai, F. Ellis, R. Thevamaran, and T. Kottos, Exceptional-point-based accelerometers with enhanced signal-to-noise ratio, Nature **607**, 697 (2022).

[36] J. Wiersig, Enhancing the sensitivity of frequency and energy splitting detection by using exceptional points: application to microcavity sensors for single-particle detection, Phys. Rev. Lett. **112**, 203901 (2014).

[37] F. Vollmer and L. Yang, Review label-free detection with high-q microcavities: a review of biosensing mechanisms for integrated devices, Nanophotonics **1**, 267 (2012).

[38] S. Sunada and T. Harayama, Design of resonant microcavities: application to optical gyroscopes, Opt. Express **15**, 16245 (2007).

[39] L. Rondin, J.-P. Tetienne, T. Hingant, J.-F. Roch, P. Maletinsky, and V. Jacques, Magnetometry with nitrogen-vacancy defects in diamond, Rep. Prog. Phys **77**, 056503 (2014).

[40] J. F. Barry, J. M. Schloss, E. Bauch, M. J. Turner, C. A. Hart, L. M. Pham, and R. L. Walsworth, Sensitivity optimization for nv-diamond magnetometry, Rev. Mod. Phys. **92**, 015004 (2020).

[41] P. Djorwe, Y. Pennec, and B. Djafari-Rouhani, Exceptional point enhances sensitivity of optomechanical mass sensors, Phys. Rev. Applied **12**, 024002 (2019).

[42] J. Chaste, A. Eichler, J. Moser, G. Ceballos, R. Rurali, and A. Bachtold, A nanomechanical mass sensor with yoctogram resolution, Nat. Nanotech. **7**, 301 (2012).

[43] E. Gil-Santos, D. Ramos, J. Martínez, M. Fernández-Regúlez, R. García, Á. San Paulo, M. Calleja, and J. Tamayo, Nanomechanical mass sensing and stiffness spectrometry based on two-dimensional vibrations of resonant nanowires, Nat. Nanotech. **5**, 641 (2010).

[44] K. Brading, E. Castellani, and N. Teh, Symmetry and Symmetry Breaking, in *The Stanford Encyclopedia of Philosophy*, edited by E. N. Zalta and U. Nodelman (Metaphysics Research Lab, Stanford University, 2023) Fall 2023 ed.

[45] T. Hollowood, Solitons in affine Toda field theories, Nucl. Phys. B. **384**, 523 (1992).

[46] T. T. Wu, Ground state of a Bose system of hard spheres, Phys. Rev. **115**, 1390 (1959).

[47] C. M. Bender and S. Boettcher, Real spectra in non-Hermitian Hamiltonians having PT symmetry, Phys. Rev. Lett. **80**, 5243 (1998).

[48] Y. Ashida, Z. Gong, and M. Ueda, Non-Hermitian physics, Adv. Phys. **69**, 249 (2020).

[49] H. Yuan, P. Yan, S. Zheng, Q. He, K. Xia, and M.-H. Yung, Steady Bell state generation via magnon-photon coupling, Phys. Rev. Lett. **124**, 053602 (2020).

[50] A. Bergman, R. Duggan, K. Sharma, M. Tur, A. Zadok, and A. Alù, Observation of anti-parity-time-symmetry, phase transitions and exceptional points in an optical fibre, Nat. Commun. **12**, 486 (2021).

[51] L. Xiao, X. Zhan, Z. Bian, K. Wang, X. Zhang, X. Wang, J. Li, K. Mochizuki, D. Kim, N. Kawakami, *et al.*, Observation of topological edge states in parity–time-symmetric quantum walks, Nat. Phys. **13**, 1117 (2017).

[52] B. Peng, Ş. K. Özdemir, F. Lei, F. Monifi, M. Gianfreda, G. L. Long, S. Fan, F. Nori, C. M. Bender, and L. Yang, Parity–time-symmetric whispering-gallery microcavities, Nat. Phys. **10**, 394 (2014).

[53] C. E. Rüter, K. G. Makris, R. El-Ganainy, D. N. Christodoulides, M. Segev, and D. Kip, Observation of parity–time symmetry in optics, Nat. Phys. **6**, 192 (2010).

[54] X. Yang, J. Li, Y. Ding, M. Xu, X.-F. Zhu, and J. Zhu, Observation of transient parity-time symmetry in electronic systems, Phys. Rev. Lett. **128**, 065701 (2022).

[55] S. Assawaworrarit, X. Yu, and S. Fan, Robust wireless power transfer using a nonlinear parity–time-symmetric circuit, Nature **546**, 387 (2017).

[56] P.-Y. Chen, M. Sakhdari, M. Hajizadegan, Q. Cui, M. M.-C. Cheng, R. El-Ganainy, and A. Alù, Generalized parity-time symmetry condition for enhanced sensor telemetry, Nat. Electron **1**, 297 (2018).

[57] Y. Liu, T. Hao, W. Li, J. Capmany, N. Zhu, and M. Li, Observation of parity-time symmetry in microwave photonics, Light Sci Appl **7**, 38 (2018).

[58] C. Shi, M. Dubois, Y. Chen, L. Cheng, H. Ramezani, Y. Wang, and X. Zhang, Accessing the exceptional points of parity-time symmetric acoustics, Nat. Commun. **7**, 11110 (2016).

[59] R. Fleury, D. Sounas, and A. Alù, An invisible acoustic sensor based on parity-time symmetry, Nat. Commun. **6**, 5905 (2015).

[60] F. Quijandría, U. Naether, S. K. Özdemir, F. Nori, and D. Zueco, Pt-symmetric circuit qed, Phys. Rev. A **97**, 053846 (2018).

[61] G.-Q. Zhang, Y.-P. Wang, and J. You, Dispersive readout of a weakly coupled qubit via the parity-time-symmetric phase transition, Phys. Rev. A **99**, 052341 (2019).

[62] M. Naghiloo, M. Abbasi, Y. N. Joglekar, and K. Murch, Quantum state tomography across the exceptional point in a single dissipative qubit, Nat. Phys. **15**, 1232 (2019).

[63] Y. Wu, W. Liu, J. Geng, X. Song, X. Ye, C.-K. Duan, X. Rong, and J. Du, Observation of parity-time symmetry breaking in a single-spin system, Science **364**, 878 (2019).

[64] Z. Zhang, Y. Zhang, J. Sheng, L. Yang, M.-A. Miri, D. N. Christodoulides, B. He, Y. Zhang, and M. Xiao, Observation of parity-time symmetry in optically induced atomic lattices, Phys. Rev. Lett. **117**, 123601 (2016).

[65] Z. Lin, H. Ramezani, T. Eichelkraut, T. Kottos, H. Cao, and D. N. Christodoulides, Unidirectional invisibility induced by PT-symmetric periodic structures, Phys. Rev. Lett. **106**, 213901 (2011).

[66] L. Chang, X. Jiang, S. Hua, C. Yang, J. Wen, L. Jiang, G. Li, G. Wang, and M. Xiao, Parity–time symmetry and variable optical isolation in active–passive-coupled microresonators, Nat. Photon **8**, 524 (2014).

[67] W. Chen, Ş. Kaya Özdemir, G. Zhao, J. Wiersig, and L. Yang, Exceptional points enhance sensing in an optical microcavity, Nature **548**, 192 (2017).

[68] M. P. Hokmabadi, A. Schumer, D. N. Christodoulides, and M. Khajavikhan, Non-Hermitian ring laser gyroscopes with enhanced sagnac sensitivity, Nature **576**, 70 (2019).

[69] C. Dembowski, H.-D. Gräf, H. Harney, A. Heine, W. Heiss, H. Rehfeld, and A. Richter, Experimental observation of the topological structure of exceptional points, Phys. Rev. Lett. **86**, 787 (2001).

[70] S.-B. Lee, J. Yang, S. Moon, S.-Y. Lee, J.-B. Shim, S. W. Kim, J.-H. Lee, and K. An, Observation of an exceptional point in a chaotic optical microcavity, Phys. Rev. Lett. **103**, 134101 (2009).

[71] T. Gao, E. Estrecho, K. Bliokh, T. Liew, M. Fraser, S. Brodbeck, M. Kamp, C. Schneider, S. Höfling, Y. Yamamoto, *et al.*, Observation of non-Hermitian degeneracies in a chaotic exciton-polariton billiard, Nature **526**, 554 (2015).

[72] C. Zeng, K. Zhu, Y. Sun, G. Li, Z. Guo, J. Jiang, Y. Li, H. Jiang, Y. Yang, and H. Chen, Ultra-sensitive passive wireless sensor exploiting high-order exceptional point for weakly coupling detection, New J. Phys. **23**, 063008 (2021).

[73] X.-G. Wang, G.-H. Guo, and J. Berakdar, Enhanced sensitivity at magnetic high-order exceptional points and topological energy transfer in magnonic planar waveguides, Phys. Rev. Applied **15**, 034050 (2021).

[74] Z. Lin, A. Pick, M. Lončar, and A. W. Rodriguez, Enhanced spontaneous emission at third-order Dirac exceptional points in inverse-designed photonic crystals, Phys. Rev. Lett. **117**, 107402 (2016).

[75] K. Ding, G. Ma, M. Xiao, Z. Zhang, and C. T. Chan, Emergence, coalescence, and topological properties of multiple exceptional points and their experimental realization, Phys. Rev. X **6**, 021007 (2016).

[76] P. Delplace, T. Yoshida, and Y. Hatsugai, Symmetry-protected multifold exceptional points and their topological characterization, Phys. Rev. Lett. **127**, 186602 (2021).

[77] I. Mandal and E. J. Bergholtz, Symmetry and higher-order exceptional points, Phys. Rev. Lett. **127**, 186601 (2021).

[78] S. Sayyad and F. K. Kunst, Realizing exceptional points of any order in the presence of symmetry, Phys. Rev. Res. **4**, 023130 (2022).

[79] J. Wiersig, Review of exceptional point-based sensors, Photonics Res. **8**, 1457 (2020).

[80] G.-Q. Zhang and J. Q. You, Higher-order exceptional point in a cavity magnonics system, Phys. Rev. B **99**, 054404 (2019).

[81] W. Xiong, Z. Li, G.-Q. Zhang, M. Wang, H.-C. Li, X.-Q. Luo, and J. Chen, Higher-order exceptional point in a blue-detuned non-Hermitian cavity optomechanical system, Phys. Rev. A **106**, 033518 (2022).

[82] S. Xia, C. Danieli, Y. Zhang, X. Zhao, H. Lu, L. Tang, D. Li, D. Song, and Z. Chen, Higher-order exceptional point and Landau–Zener Bloch oscillations in driven non-hermitian photonic Lieb lattices, APL Photonics **6** (2021).

[83] J. L. Barnett, Locality and exceptional points in Pseudo-Hermitian physics, arXiv preprint arXiv:2306.04044 (2023).

[84] R. Benzi, A. Sutera, and A. Vulpiani, The mechanism of stochastic resonance, J. Phys. A: Math. Gen. **14**, L453 (1981).

[85] L. Gammaitoni, P. Hänggi, P. Jung, and F. Marchesoni, Stochastic resonance, Rev. Mod. Phys. **70**, 223 (1998).

[86] J. J. Collins, C. C. Chow, and T. T. Imhoff, Stochastic resonance without tuning, Nature **376**, 236 (1995).

[87] F. J. Castro, M. N. Kuperman, M. Fuentes, and H. S. Wio, Experimental evidence of stochastic resonance without tuning due to non-gaussian noises, Phys. Rev. E **64**, 051105 (2001).

[88] K. Park, Y.-C. Lai, and S. Krishnamoorthy, Noise sensitivity of phase-synchronization time in stochastic resonance: Theory and experiment, Phys. Rev. E **75**, 046205 (2007).

[89] Y.-C. Lai, K. Park, and L. Rajagopalan, Stochastic resonance and energy optimization in spatially extended dynamical systems, Eur. Phys. J. B **69**, 65 (2009).

[90] L. Ying, L. Huang, and Y.-C. Lai, Enhancing optical response of graphene through stochastic resonance, Phys. Rev. B **97**, 144204 (2018).

[91] G. Krishnan, C. U. Kshirsagar, G. Ananthasuresh, and N. Bhat, Micromachined high-resolution accelerometers, J. Indian Inst. Sci. **87**, 333 (2007).

[92] Y. Shindo, T. Yoshikawa, and H. Mikada, A large scale seismic sensing array on the seafloor with fiber optic accelerometers, in *SENSORS, 2002 IEEE*, Vol. 2 (IEEE, 2002) pp. 1767–1770.

[93] M.-H. Bao, *Micro Mechanical Transducers: Pressure Sensors, Accelerometers and Gyroscopes* (Elsevier, 2000).

[94] W. Wu, Z. Li, J. Liu, J. Fan, and L. Tu, A nano-g mems accelerometer for earthquake monitoring, in *2017 19th International Conference on Solid-State Sensors, Actuators and Microsystems (TRANSDUCERS)* (IEEE, 2017) pp. 599–602.

[95] Z. Li, W. J. Wu, P. P. Zheng, J. Q. Liu, J. Fan, and L. C. Tu, Novel capacitive sensing system design of a microelectromechanical systems accelerometer for gravity measurement applications, Micromachines **7**, 167 (2016).

[96] C. Malmberg and A. Maryott, Dielectric constant of water from 0 to 100 c, J. Res. Natl. Inst. Stand. Technol. **56**, 1 (1956).

[97] C. Li, Q. Tan, C. Xue, W. Zhang, Y. Li, and J. Xiong, A high-performance LC wireless passive pressure sensor fabricated using low-temperature co-fired ceramic (LTCC) technology, Sensors **14**, 23337 (2014).